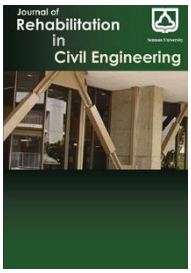

journal homepage: http://civiljournal.semnan.ac.ir/

# An Investigation of Performance of Masonry Wall Reinforced with Timber lumbers

**M. Mohammadi Nikoo[1*], A.H. Akhaveissy[2], A. Permanoon[3]**

1. Ph.D. Student of Structural Engineering, Faculty of Engineering, Khajeh Nasir Toosi University of Technology (KNTU), Tehran, Iran.
2. Assistant Professor of Civil Engineering, Faculty of Engineering, Razi University, Kermanshah, Iran.
3. Ph.D. Student of Structural Engineering, Faculty of Engineering, Razi University, Kermanshah, Iran.

Corresponding author: *m.mohamadi30@ymail.com*

**ARTICLE INFO**

Article history:
Received: 13 December 2017
Accepted: 10 November 2020

Keywords:
Timber Properties,
Mechanical Testing,
Masonry Wall,
Meso Scale,
Constitutive Law.

**ABSTRACT**

The current article seeks to investigate the behavior of masonry wall reinforced with timber lumbers and effect of timbers on increasing the shear strength and ductility of wall. To determine the mechanical properties of the timbers, two experiments according to ASTM D143 were performed. All of the mechanical properties required for timber simulation were determined via tensile and compressive tests, and using parametric equations. The behavior of the timbers under tensile force was brittle, and under pressure was semi-ductile. Hill yield criterion was utilized for timber behavior modelling. Predictably, the location of the plastic strain formation in the tensile and compressive specimen was consistent with the location of the fracture in the experimental specimens. In the next parts of the research, the obtained parameters were used to model the mechanical behavior of the timbers. Macro and meso approaches were used for the numerical modeling of the masonry wall. The Willam–Warnke yield criterion was used on the macro scale, and the cohesive-frictional interface constitutive model was utilized on the meso scale. Both numerical models were in good agreement with the laboratory results. However, due to the gap and sliding of the masonry wall in the numerical model, the Meso scale was used in the research. The masonry wall was retrofitted and strengthened by three different patterns of timber placement. An examination of the analysis results showed that by placing the timbers, the wall cracking pattern tends to change, and the ductility and shear capacity of the wall considerably enhances.

DOI: 10.22075/JRCE.2020.13379.1243

## 1. Introduction

During earthquakes, timber structures have proved to bring about an acceptable performance thanks to their high ratio between strength and mass [1]. They exhibit excellent performance if all structural members and details are designed and constructed correctly[2]. Timber structures in European seismic areas are found as building frames, in combination with masonry infills [3].

The research on connecting and strengthening timber structural elements with glued-in rods (GiR), has been considered in this work by theoretical approaches to estimate their load-bearing capacity and existing design recommendations [4].

Anil et al. developed a model with a fictive diagonal for quick and accurate determination of racking stiffness of composite timber-framed wall elements [5].

Bedon et al. investigated the non-linear modelling of the cyclic behavior of Blockhaus timber log-walls under in-plane lateral loads. They confirmed that the proposed modelling approach can be used to estimate the load-carrying capacity and vulnerability to seismic events of Blockhaus shear walls [6].

The main objectives of Guíñez, F. and et al. research are to evaluate the seismic response of these shear walls and to assess the current code expressions applied to shear walls with sturdy end studs to be used in mid-height timber buildings [7].

In 2020, according to the ‘design by testing’ approach, regression analyses have been carried out on the whole database in order to assess new formulations taking into account the most important parameters influencing the performance of injected anchors made of both traditional and innovative materials [8].

Estrella, X., and et al. presented an efficient nonlinear modeling approach to better understand such behavior under large displacement demands. They show that redesigning the nailing pattern can increase the capacity of strong wood frame walls [9].

The static and dynamic response of cross-laminated timber (CLT) composites combined with reinforced concrete (RC), hollow steel profiles and laminated strand lumber (LSL) are investigated in [10].

A light-frame timber shear wall (LFTSW) with OSB sheathing stapled to glued-laminated timber framing and strong anchorages are investigated in this research program to be used as the single lateral load resisting system being located in the perimeter of the building [11].

Jayamon, J. R., and et al. provided the development of rational damping models and improved procedures for the analysis of wood-frame shear wall structures [12].

The seismic low-cyclic fatigue strength for different typologies of dissipative timber connections is analyzed by means of a novel methodology, which defines an interaction between the strength degradation and ductility capacity [13].

In the present paper, using parametric equations and experimental results, the mechanical properties of timbers were determined, and then timber specimens were modeled in **ANSYS** finite element software. After validating the timber element modelling, the masonry wall was simulated via macro and meso approaches.

To validate the brick wall modeling, cracking patterns and load-displacement diagram were investigated.

Then, after validating the simulations, the brick walls were reinforced with timber. The results of the analysis showed that the timbers increase the load bearing capacity and wall ductility by changing the wall cracking pattern.

## 2. Determine the mechanical properties of the specimens

### 2.1. Tension Parallel to Timber Grain Test and Compression Perpendicular to Timber Grain Test

Tensile and compressive specimens were prepared according to ASTM D143-14 standard [14]. Some mechanical properties of timber can be measured by performing two tests including Tension Parallel to Timber Grain Test and Compression Perpendicular to Timber Grain Test. The dimensions of the experimental specimens are shown in Figure 1.

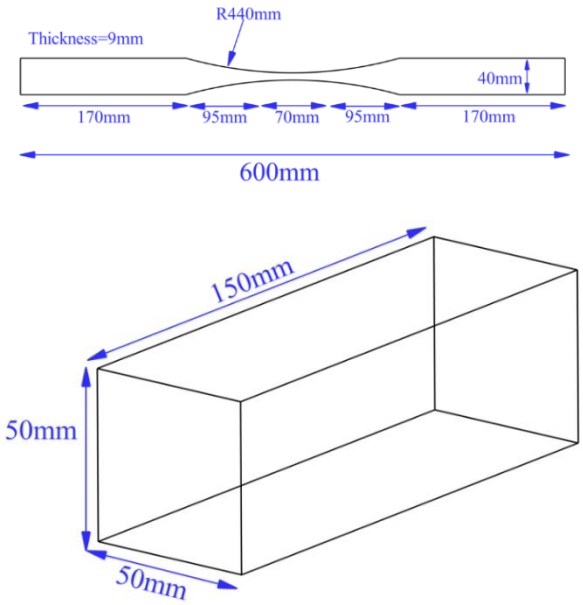


**Fig. 1.** Standard Specimen Dimensions.

For Tension Parallel to Timber Grain Test and Compression Perpendicular to Timber Grain Test, 3 specimens were prepared and tested. The experimental specimens are shown in Figure 2. The tensile specimens ($W_1 - W_2 - W_3$) are completely restrained by the jack opening. The test was performed in a displacement-control form, and the displacement reading was recorded by an extensometer. According to the ASTM D143 standard, displacement was applied to the specimens at a speed of 1 mm/min, and the reading accuracy of the deformations was 0.002mm.

The compressive specimens ($S_1$- $S_2$- $S_3$) below the jack were tested under displacement control, and loading was performed at a speed of 0.305mm/min according to the ASTM D143 standard.

The stress-strain diagram of the compressive and tensile specimens is shown in Figure 3. The stress-strain diagram of the numerical specimens clearly indicates that the tensile behavior of the timber aligned with the fiber is quite brittle. This is probably due to the rupture of the fibers. Concurrent with the loss of tensile fibers, the strength decreases promptly. The behavior of the compressive specimens is in the form of quasi-ductile materials, and when the timber approaches its maximum resistance, the resistance gradually declines. Therefore, the behavior of the timber under tensile force is brittle, and is semi-ductile under pressure. Then, by examining the stress-strain diagram of the tensile and compressive testing, the modulus of elasticity of the tensile specimens were calculated to be 9560, 9760 and 10059 MPa, respectively, and the modulus of elasticity of the compressive specimens to be 17456, 17680 and 17375, respectively.


**Fig. 2.** Tensile and compressive specimens under Tension Parallel to Timber Grain Test and Compression Perpendicular to Timber Grain Test.

On the other hand, the modulus of elasticity of the tensile specimens was obtained to be 9805 Mpa, and modulus of elasticity of the compressive specimens to be 17500 Mpa.

The mean stress value in the tensile speciemens was 58 MPa, and the average stress in the compressive specimens was 6 MPa.

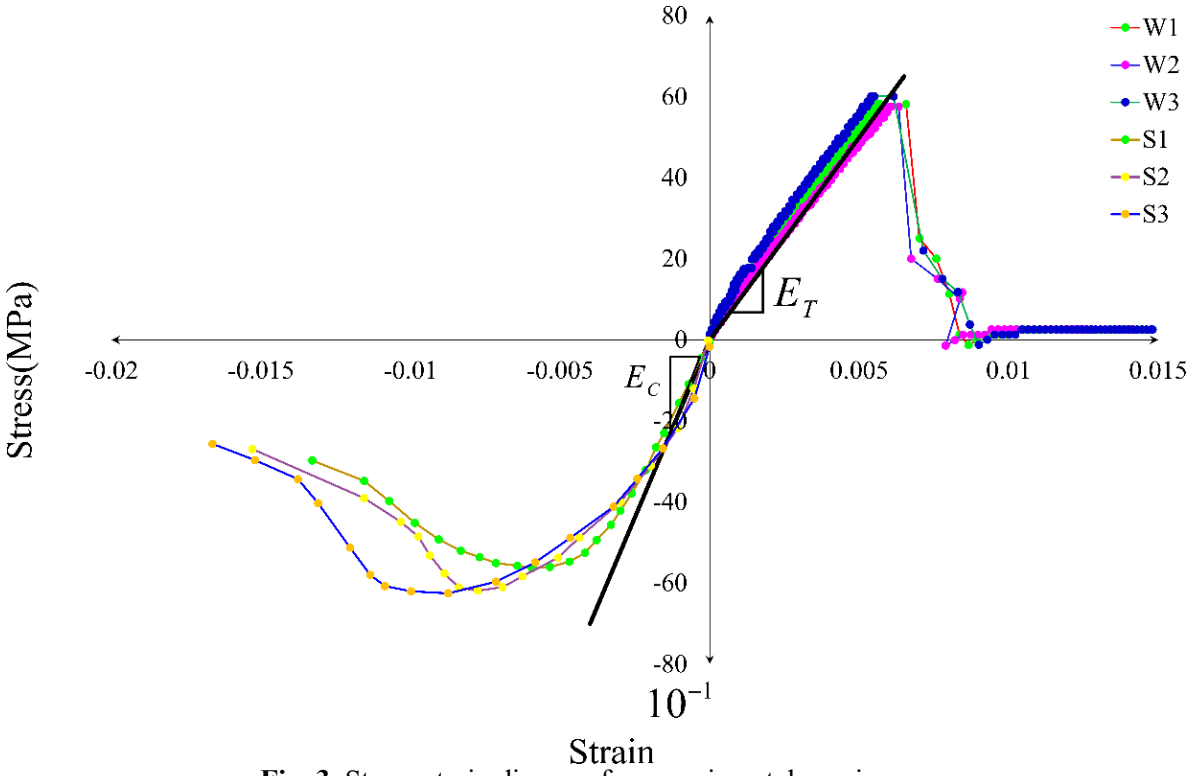


**Fig. 3.** Stress-strain diagram for experimental specimens.

The following equations were used to determine other mechanical properties of the timber specimens. Poisson's ratio values for sycamore wood parallel to the fibers is recommended to be 0.025, and in the direction perpendicular to the fibers to be 0.45 [15].

The relationship between Poisson's coefficients and the elastic modulus is given in Equation 1, where L is the direction parallel to the fiber and T is the direction perpendicular to the fiber, and E is the compressive modulus of elasticity or the base modulus in MPa, and ν is the Poisson's ratio.

$$\frac{\nu_{TL}}{\nu_{LT}} = \frac{E_T}{E_L} \quad (1)$$

After determining Poisson's coefficients and modulus of elasticity, shear modulus of different directions in the timber specimens can be calculated, and Equation 2 shows the relations between them. Here, G is the shear modulus whose unit is MPa.

$$G_{TL}, G_{LT} = \frac{\sqrt{E_L . E_T}}{2(1+\sqrt{\nu_{TL} . \nu_{LT}})} \quad (2)$$

In order to calculate the shear yield stresses, both shear modulus and shear yield strains in the bilinear stress-strain curves must be calculated. Equation 3 shows the procedure to calculate shear yield strains and shear

yield stresses in the timber specimens, in which $\gamma_y$

is the shear yield strain, $\sigma_0$ is the compressive yield stress perpendicular to the fiber axis, and $E_t$ is the tangential modulus equal to (0.01 ˣE) [16].

$$(\gamma_y)_{TL},(\gamma_y)_{LT} = \frac{(\sigma_0)_T}{2(E_T-(E_t)_T)}\sqrt{\frac{E_T}{G_{TL}}} \quad (3)$$

$$\tau_{TL}=\tau_{TR}=(\gamma_y)_{TL}\times G_{TL}$$

According to Equation 4, using Poisson's ratios and modulus of longitudinal elasticity, modulus of radial and tangential elasticity, shear modulus, and shear yield stresses can be extracted.

$$equation(1)\Rightarrow \frac{0.025}{0.45}=\frac{E_T}{9805}\Rightarrow E_T=E_R=544.72(MPa)$$

$$equation(2)\Rightarrow \begin{cases} G_{TL}=G_{RL}=\dfrac{\sqrt{9805\times 544.72}}{2(1+\sqrt{0.024\times 0.45})}=1046.54 \\ G_{TR}=\dfrac{\sqrt{544.72\times 544.72}}{2(1+\sqrt{0.024\times 0.024})}=265.6 \end{cases} \quad (4)$$

$$equation(2)\Rightarrow \begin{cases} (\gamma_y)_{TL}=\dfrac{60}{2(17500-17500\times 0.01)}\sqrt{\dfrac{17500}{1046.54}}=0.0068 \\ \tau_{TL}=0.0068\times 1046.45=7.11(MPa) \end{cases}$$

## 3. Numerical model validation

### 3.1. Orthotropic behavioral model of wood

Hill yield criterion was used to model the numerical behavior of the timber [17]. Such yield was developed based on Von Mises yield criterion, and can consider orthotropic behavior in different directions.

The formulation of this yield criterion in the stress space is presented in Equation 5.

$$f(\sigma,\sigma_y)=F(\sigma_{22}-\sigma_{33})^2+G(\sigma_{33}-\sigma_{11})^2+H(\sigma_{11}-\sigma_{22})^2$$
$$+2L\sigma_{23}^2+2M\sigma_{31}^2+2N\sigma_{12}^2-\sigma_y^2=0$$
$$F=\frac{1}{2}\left(\frac{1}{R_{22}^2}+\frac{1}{R_{33}^2}-\frac{1}{R_{11}^2}\right),\ G=\frac{1}{2}\left(\frac{1}{R_{33}^2}+\frac{1}{R_{11}^2}-\frac{1}{R_{22}^2}\right),\ H=\frac{1}{2}\left(\frac{1}{R_{11}^2}+\frac{1}{R_{22}^2}-\frac{1}{R_{33}^2}\right)$$
$$L=\frac{3}{2}\left(\frac{1}{R_{23}^2}\right),\ M=\frac{3}{2}\left(\frac{1}{R_{13}^2}\right),\ N=\frac{3}{2}\left(\frac{1}{R_{12}^2}\right) \quad (5)$$
$$R_{11}=\frac{\sigma_{11}^y}{\sigma_y},\ R_{22}=\frac{\sigma_{22}^y}{\sigma_y},\ R_{33}=\frac{\sigma_{33}^y}{\sigma_y}$$
$$R_{12}=\sqrt{3}\frac{\sigma_{12}^y}{\sigma_y},\ R_{23}=\sqrt{3}\frac{\sigma_{23}^y}{\sigma_y},\ R_{13}=\sqrt{3}\frac{\sigma_{13}^y}{\sigma_y}$$

$\sigma_y^i$ is the yield stress value in different directions. 3-D **SOLID185** was used to model the tensile and compressive specimens. This element has three degrees of transfer freedom in each node (Figure 4).

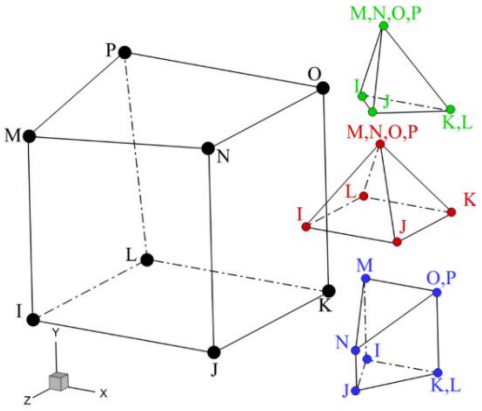


**Fig. 4.** 3-D SOLID185.

Figure 5 shows meshing procedure for the numerical specimens and boundary conditions. To accurately model the compressive behavior between the timber and steel supports, a contact element was used to model the loading correctly. Furthermore, Figure 5 presents the strain distribution in the XX and YY directions for the tensile and compressive specimens, respectively.

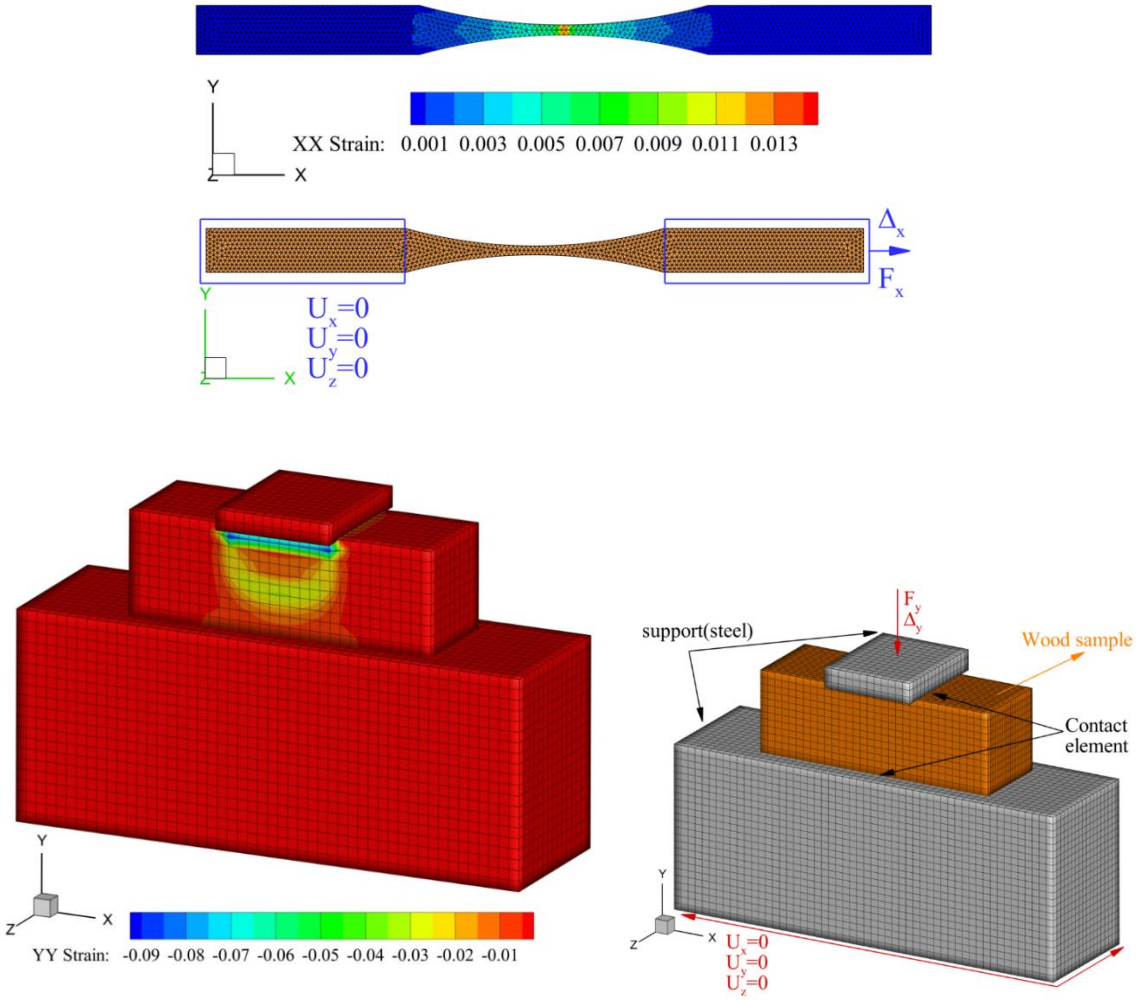


**Fig. 5.** a) Tensile specimen and plastic strain in the direction of fibers b) Compressive specimen and plastic strain in the direction perpendicular to the direction of the fibers.

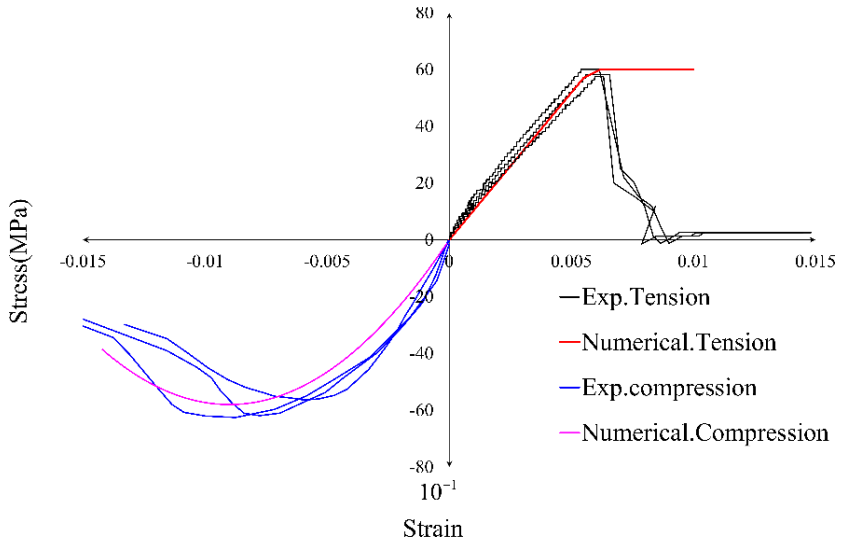


**Fig. 6.** Comparison of the results of numerical model and experimental specimens.

A good agreement can be observed between the stress-strain diagrams of the numerical and experimental specimens. As expected, the location of the plastic strain formation in the tensile and compressive specimens corresponds to the fracture site in the experimental specimens (Figure 5). After validating the behavioral model for the timber, the following parameters were used to model the mechanical behavior of the timber.

**Table 1.** Mechanical properties of timber.

| Material parameters for timber | |
|---|---|
| Elastic modulus L (MPa) | 9805(MPa) |
| Elastic modulus R, T (MPa) | 544.7(MPa) |
| Elastic shear modulus RL, LT (MPa) | 1046(MPa) |
| Elastic shear modulus RT (MPa) | 265(MPa) |
| Poisson's ratio RL | 0.024 |
| Poisson's ratio LT | 0.45 |
| Poisson's ratio RT | 0.45 |
| Compressive, tensile yield stress R, L, T (MPa) | 6-58-6(MPa) |
| Shear yield stress RL, LT, RT (MPa) | 7.11-7.11-1.3(MPa) |

## 3.2. Behavioral model of masonry wall

To determine the parameters of the masonry wall, the mechanical characteristics of the shear wall proposed by Wermeltfort et al. were used. This masonry wall has been studied by many researchers. The mechanical properties of the wall are shown in Table 2 [18].

**Table 2.** Mechanical characteristics of the shear wall proposed by Wermeltfort et al. [18].

| | E(GPa) | ν | $f_t$ | $f_c$ |
|---|---|---|---|---|
| Masonry | 8000 | 0.15 | 0.25 | 10.5 |
| Brick | 16700 | 0.15 | 2 | - |

The geometry and boundary conditions of the wall are given in Figure 7. The wall consists of single layer of solid bricks (210mm*52mm*100mm), and 10 mm of mortar [19, 20]. Loading conditions are applied in two stages. In the first stage, the top of the wall is subjected to a uniform vertical compression. In the second stage, a horizontal force is applied via displacement control, while keeping the top of the wall horizontal. The experimentally obtained crack patterns are shown in Figure 8. Two tests were performed for the mentioned masonry wall. The load-displacement diagram of the horizontal wall is shown in Figure 13.

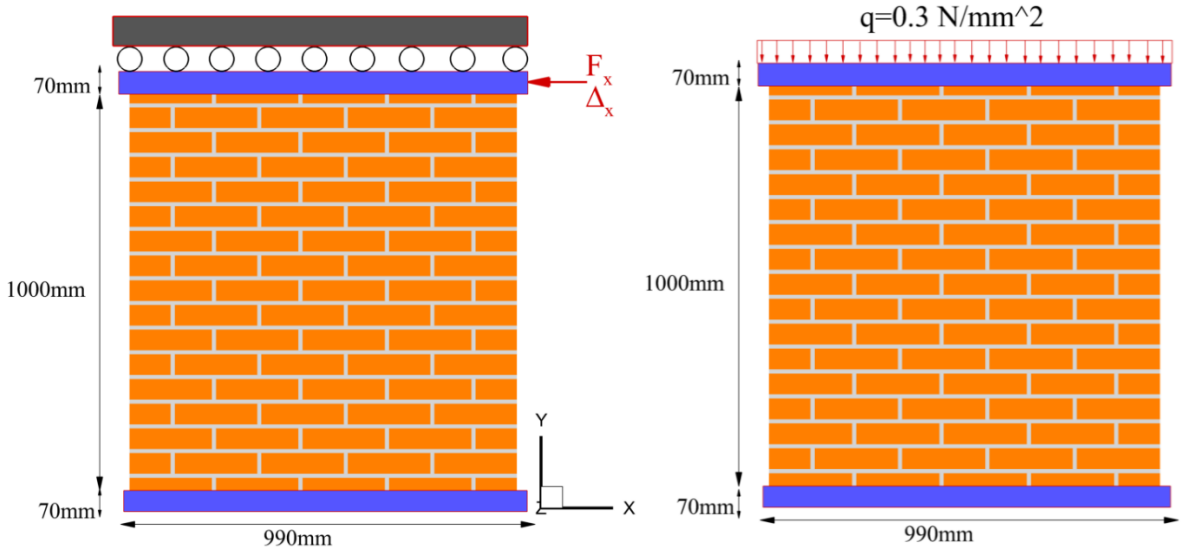


**Fig. 7.** Dimensions and loading and support conditions of shear wall.

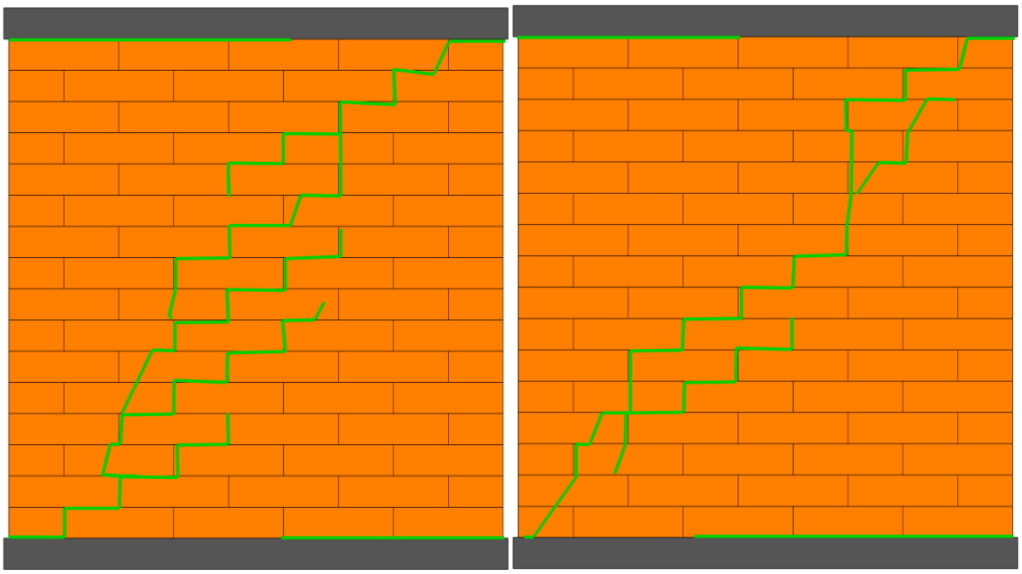

**Fig. 8.** Cracking in the experimental wall.

For numerical modeling of the masonry wall [19, 20], macro and meso approaches were used to completely validate the numerical model selected for the masonry wall, and to select a more suitable model for performing the next steps of the research.

To analyze the numerical models, first a vertical load (0.3 MPa), and then a horizontal load was applied.

3.2.1. Macro model

For macro-scale modeling, the properties of the building unit were used, since its mechanical characteristics involves properties of brick and mortar. A suitable yield level for brittle material modelling is the Menétrey-Willam Yield Criterion. This criterion considers the behavior in tension and pressure as shown in Figure 9. Further details on the criterion can be found in[21, 22].

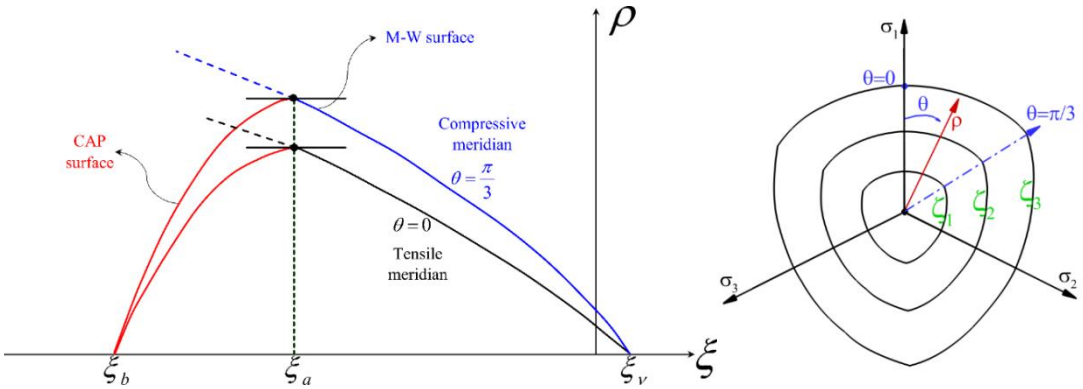


**Fig. 9.** 3D Menetrey-Willam Yield Criterion a) Tensile and compressive cap, b) In 3-D space.

According to Table 3, the following parameters were used for the macro-scale numerical model. The meshing and cracking pattern of the macro model are shown in Figure 10.

**Table 3.** Mechanical properties of wall in macro model

| | E(GPa) | ν | $f_t$ | $f_c$ |
|---|---|---|---|---|
| Macro Model | 8000 | 0.15 | 1.05 | 10.5 |

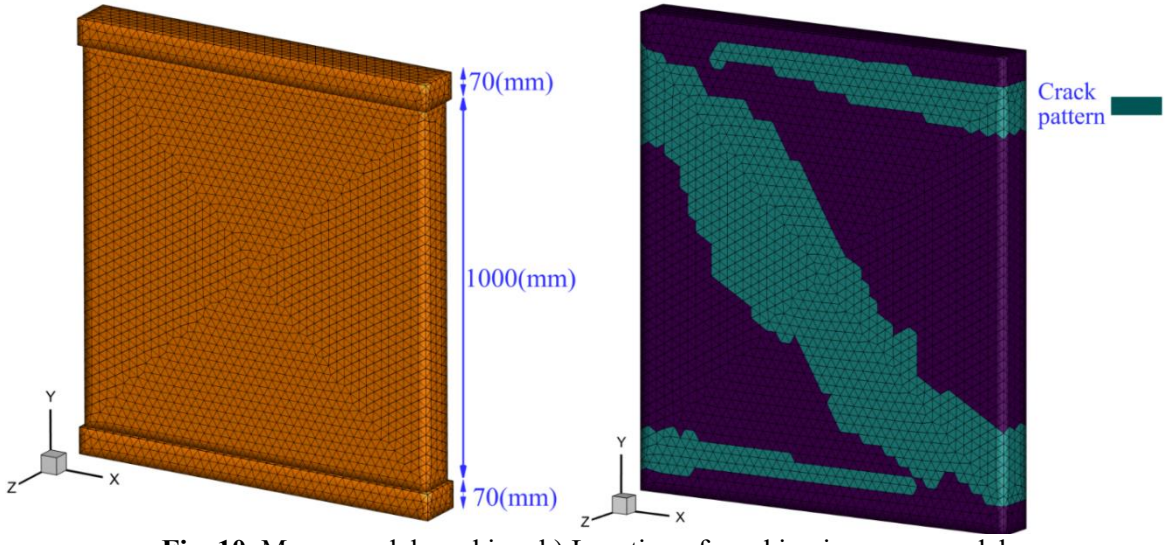


**Fig. 10.** Macro model meshing, b) Location of cracking in macro model.

As can be seen, the cracking of the numerical model on the macro scale is in good agreement with the experimental results. The load-displacement diagram of the numerical model on the macro scale is shown in Figure 13. The initial stiffness and maximum load values are almost the same as the experimental results. One disadvantage of this model is that it does not consider sliding between bricks and mortar, but instead the model has a lower computational cost (cpu time) than the numerical model on the meso scale.

### 3.2.2. Meso scale building model

To validate the numerical model and select an appropriate model, the masonry wall was also modeled on the meso scale to be able to select the best parameter for the mechanical properties of the masonry wall. The masonry wall[20] was modeled on the meso scale using the parameters presented in Table 4 [20].

**Table 4.** Mechanical properties of wall on meso scale [20].

| | E | v | $F_c$ | $F_t$ | $G_I$ | $G_{II}$ | ϕ | C | $K_n$ | $K_t$ |
|---|---|---|---|---|---|---|---|---|---|---|
| Brick | 16700 (MPa) | 0.15 | 10.5 (MPa) | 2 (MPa) | - | - | - | - | - | - |
| Interface element (mortar) | 8000 | 0.14 | | 0.25 (MPa) | 0.016 $N/mm$ | 0.125 $N/mm$ | 37° | 0.35 (MPa) | 82 $N/mm^3$ | 36 $N/mm^3$ |

The CZM model was used to model the mortar and to consider the adhesion between the mortar and the brick as well as the sliding between them[23]. In this method, sliding and gap are modeled based on the stress-gap law. Further details on the CZM model can be found in[24, 25]. Based on Figure 11, in CZM model, the bilinear model and he *Coulomb* Friction Model are used to calculate the normal and shear stresses between the elements (Equation 6).

$$\sigma = \begin{cases} \dfrac{\bar{\sigma}}{\delta_n^0}\delta_n, & \text{if } \delta_n < \delta_n^0 \\ \dfrac{\delta_n^1 - \delta_n}{\delta_n^1 - \delta_n^0}\bar{\sigma}, & \text{if } \delta_n^0 < \delta_n < \delta_n^1 \\ 0, & \text{if } \delta_n \geq \delta_n^1 \end{cases}$$

$$|\tau| = \begin{cases} \dfrac{\delta_t}{\delta_t^0}(\bar{\tau} + \tau_f), & \text{if } |\delta_t| < \delta_t^0 \\ \dfrac{\delta_t^1 - \delta_t}{\delta_t^1 - \delta_t^0}(\bar{\tau} + \tau_f), & \text{if } \delta_t^0 < |\delta_t| < \delta_t^1 \\ \tau_f, & \text{if } |\delta_t| \geq \delta_t^1 \end{cases} \quad (6)$$

$$\tau_f = \begin{cases} -\mu\sigma & \text{if } \sigma<0 \\ 0 & \text{if } \sigma<0 \end{cases}$$

$\bar{\sigma}.\bar{\tau}$ are the shear and tensile strength of the contact element, $\delta_n.\delta_t$ are the values of the gap of the contact element in the normal and shear directions, respectively.

Further, $\delta_n^0.\delta_t^0$ are the normal and shear values of the first permanent gap, $\delta_n^0.\delta_t^0$ are the normal and shear values of the displacement at the end of failure. The yield

level grade II was used to combine fracture modes[26, 27].

$$D = \sqrt{(\frac{G_I}{G_{IC}})^2 + (\frac{G_{II}}{G_{IIC}})^2} \quad (7)$$

$G_{IC}.G_{IIC}$ are critical energy release rate in tension and shear (fracture toughness), respectively. $G_{IC}.G_{II}$ are the amount of energy absorbed in the normal and shear directions, respectively. Finally, according to Equation 7, D, i.e. damage index, is in the range of 0 to 1. For nonlinear behavior of bricks, the Menétrey-Willam Yield Criterion was used, and further details on the method were explicated in the sub-section (3.2.1).

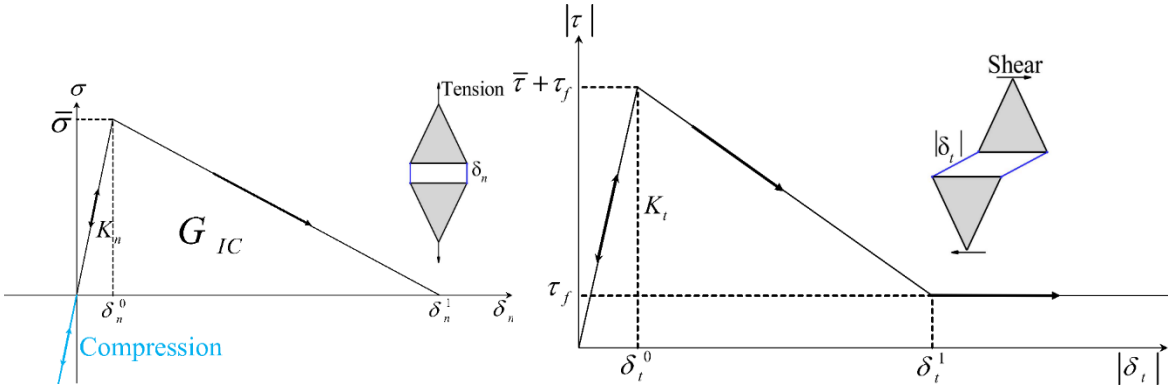


**Fig. 11.** CZM model a) under tensile force b) under shear force.

The masonry wall on the meso scale was analyzed in two steps. First, 0.3 MPa pressure was applied, and then the wall was subjected to lateral load despite the vertical load. The patterns of meshing, cracking, and sliding between the bricks are shown in Figure 12.

The cracking pattern is in a good agreement with the experimental cracking pattern. Additionally, the displacement-load diagram clearly shows that there is an acceptable consistency between modeling on the meso scale with the experimental results.

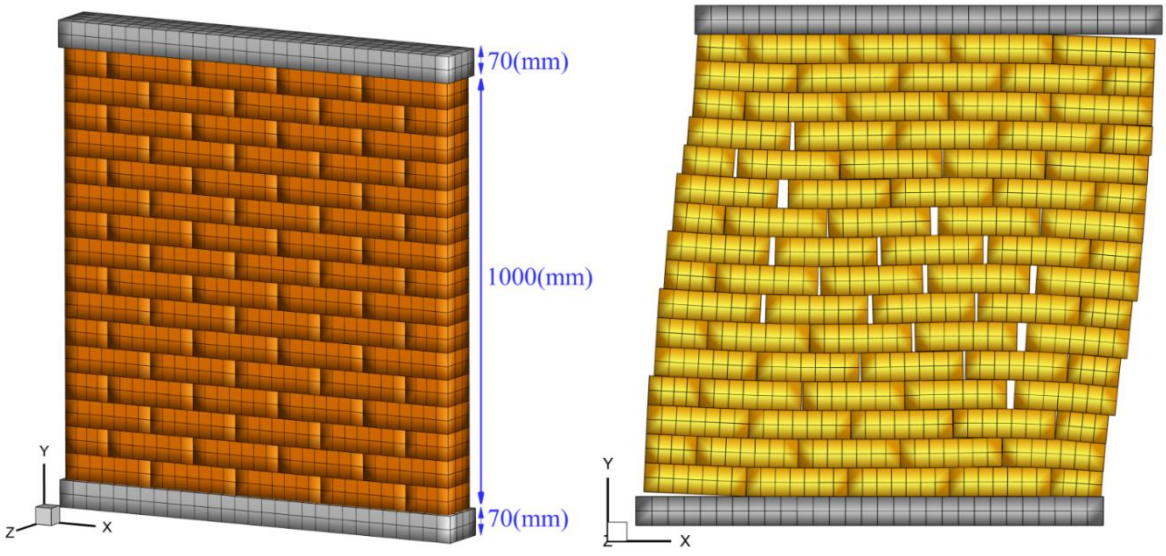


**Fig. 12.** Numerical model meshing on meso scale b) Cracking and sliding (20x).

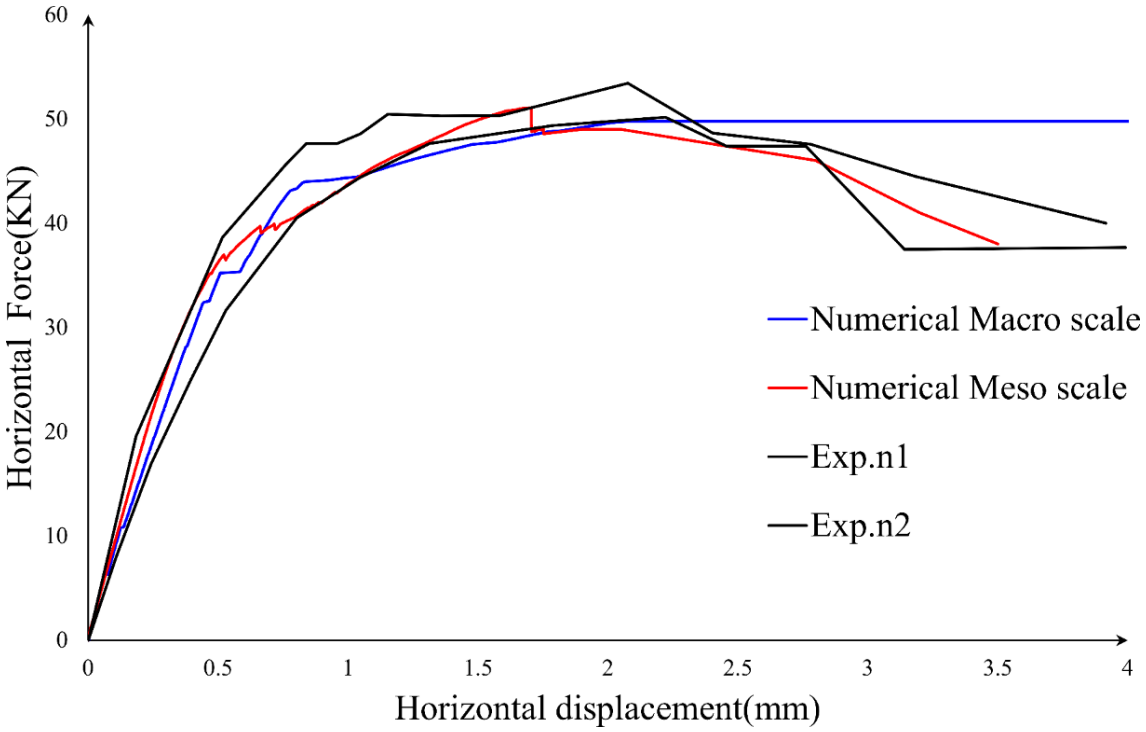


**Fig. 13.** Comparison of load-displacement diagram of numerical model on macro/meso scale and experimental results.

A comparison of the results of the two numerical models on the macro and meso scales indicates that the accuracy of the numerical model on the meso scale is higher, and has greater ability to model the masonry wall behavior. Thus, the numerical model on the meso scale is used in the following parts of the research.

## 4. Masonry wall reinforcement using timber

In this section, given the reliability of numerical models to simulate timber and wall behavior, the masonry wall was improved and strengthened by 3 different models:

1- Use of timber in the middle of the wall as a bond beam.

2- Use of timber in the middle of the wall vertically.

3- Use of timber in a crosswise form.

It should be noted that for the adhesion and friction between the timber and the masonry wall, according to the research[28], the coefficient of friction between the timber and the wall was considered to be 0.64.

This friction was considered according to the Mohr-Coulomb Criterion, and the timber slides when reaching the shear strength of mortar ($\tau_{max}$) (note: the initial adhesion value was considered to be zero; C = 0). To prevent relative movement between the timber and the wall, the cutter was used in the place of vertical and horizontal ridges (Figure 14). This system is also used in executive methods.

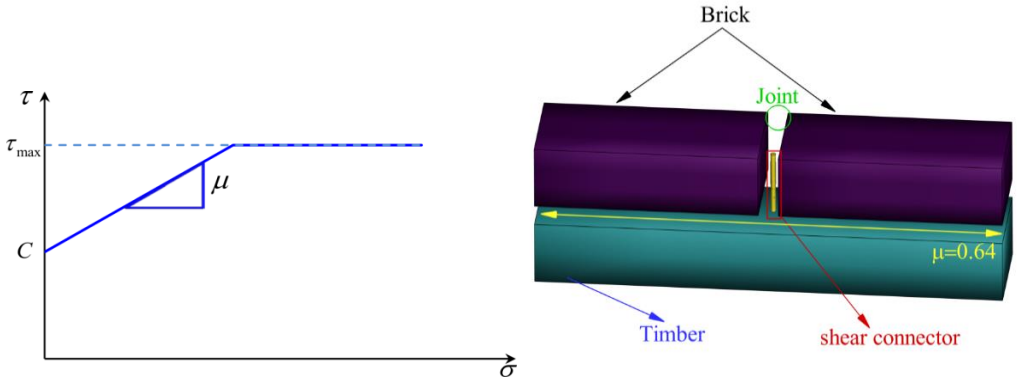


**Fig. 14.** Schematic diagram of connection of timber to brick & mortar b) Mohr–Coulomb (MC) Friction Model.

The timber used in the numerical models has a cross-sectional area (100 x 62.5) and a length commensurate with the length or width of the wall.

## 4.1. Application of timber in the middle of the wall as a bond beam

The current research mainly aims to investigate the effect of timber on behavior of masonry structures. According to previous research, by placing a bond beam in the wall, the dimensional ratio of the wall $H/L \Rightarrow h_1/L$ decreases[19], and the strength of the wall raises accordingly. Bond beam prevents the occurrence of cracking in the principal shear, and the cracking is forced to occur in a shorter length.

These changes contribute to an increase in the strength of the wall (Figure 22). According to the equations presented by Akhaveissy in 2013[19], the strength of the unreinforced masonry wall whose mechanical characteristics are presented in Table 4 and dimensional characteristics in Figure 7 is determined on the basis of Equation 8:

$$
\begin{aligned}
&P = 0.88\alpha P_U \\
&P_U = \tau_u \times L \times t + F_t \times t \times x_{\min} \\
&\tau_u = C + \sigma_0 \tan(\varphi) \\
&x_{\min} = \min \begin{cases} L \times \tan(\theta) \\ (1-\tan(\theta)) \times h \end{cases} \\
&\theta = 0.5 \tan^{-1}\left(\frac{2\tau_u}{\sigma_0}\right)
\end{aligned}
\tag{8}
$$

α is dimensionless coefficient for the for the effect of height to length ratio.

In Equation (8), α is obtained from Figure (15), θ is the angle of the principal plane; $\sigma_0$ is the initial pressure on the top of the wall; C and φ are the cohesion and the friction angle of the mortar joints, respectively; L and h are the width and the height of the wall, respectively; and $F_t$ is the tensile strength of the mortar joints. $P_U$ is the resistant lateral force; $x_{min}$ is the effective length of the wall in tension (see Figure 15); L is the width of the wall; t is the thickness of the wall; $\tau_u$ is the ultimate shear strength, which can be calculated by the Mohr-Coulomb criterion;

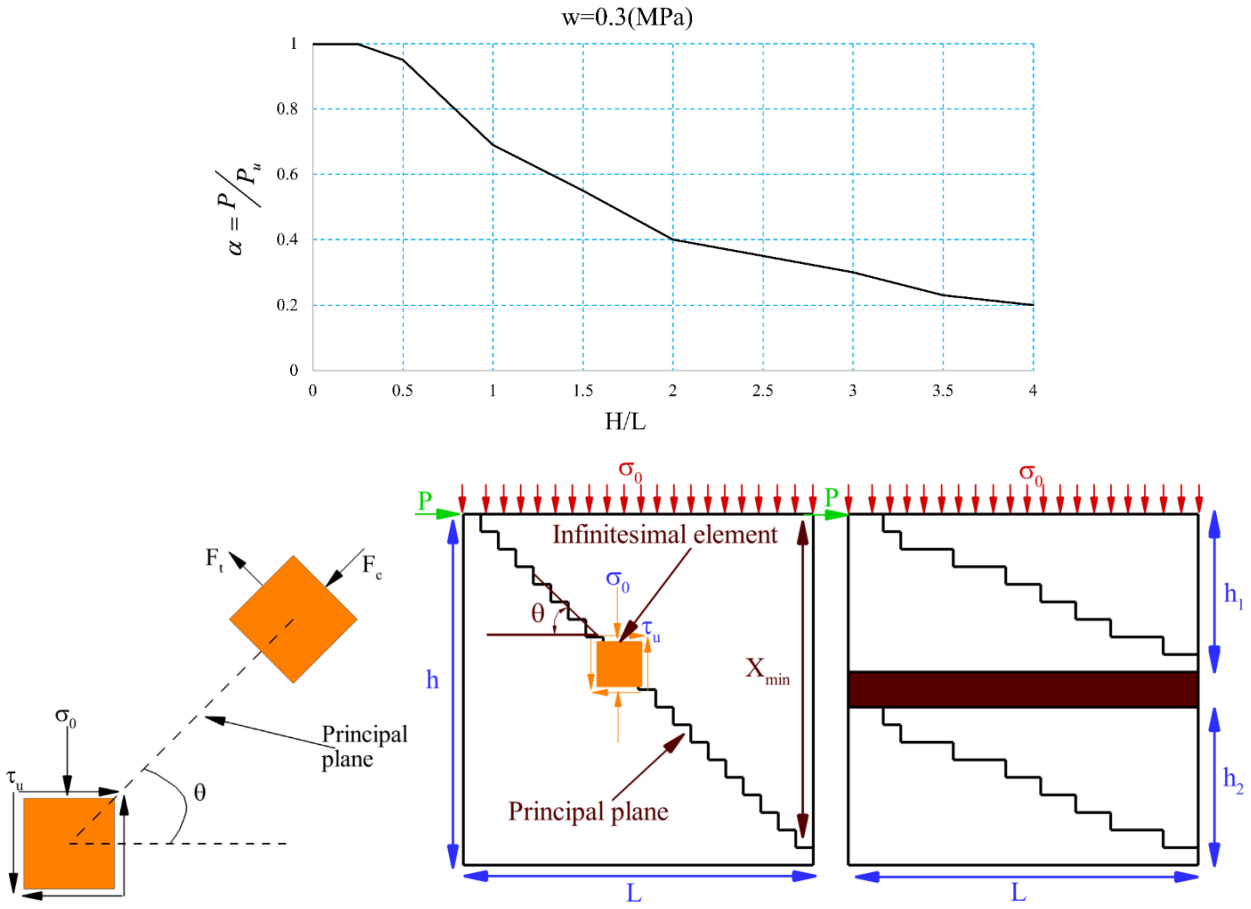


**Fig. 15.** Mechanism.

By placing timber as a bond beam in the wall, the free height of the wall amounts to $h_1$ = 500, and the wall is divided into 2 separate parts, and the total strength of the wall is the sum of the resistance of the wall at the lower and upper part of the timber. Thus, on the basis of analytical equation 8, the strength of the reinforced wall is calculated according to Table 5:

**Table 5.** A comparison of experimental results and analytic equations in reinforced wall.

| | $h/L$ | $\sigma_0(MPa)$ | $\tau_u(MPa)$ | $\theta$ | $x_{min}(mm)$ | α | P (KN) Eq. (8) | P (KN) Numerical |
|---|---|---|---|---|---|---|---|---|
| Unreinforced Masonry wall | $\frac{1000}{990}=1.01$ | 0.3 | 0.5761 | 37.7 | 227.1 | 0.707 | 39.02 | 51 |
| Reinforced Masonry wall (horizontal timber) | $\frac{500}{990}=0.505$ | 0.3 | 0.5761 | 37.7 | 113.5 | 0.707 | $37.25\times2=74.5$ | 80 |

The results clearly indicates that the timber prevents the occurrence of the shear cracking, and the shear cracking in the upper and lower parts of the timber are created in a shorter length. This timber performance enhances the strength of the wall, and lower and upper parts of the wall operate separately, and reach the maximum capacity. Figure 17 shows the wall meshing, the location of the timber, the location of the cutters between the timber and the wall, and the wall cracking. The load-displacement diagram of the wall with horizontal bond beam indicates that the wall capacity has increased by approximately 56%, and the amount of wall ductility increased considerably. According to Table 5, based on the analytical and numerical equations, the maximum load values are almost the same. This similarity is another justification for the correctness of numerical analyzes, and it is possible to calculate the wall capacity in case of existence of the bond beam without numerical calculations. However, these relations are reliable if the bending capacity of the timber meets the load applied to the wall. As seen in Figure 16, when the timber capacity reaches the maximum value, bending cracks are created at the points A and B. Accordingly, the timber must be designed for the anchorage of the point A. Therefore, the anchorage value of the timber design is calculated from Equation 9:

$$\begin{aligned} W &= R_1 \sin\theta_1 \\ R_1 &= P\cos\theta_1 \\ W &= P\tan\theta_1 \\ M_A &= (P\tan\theta_1)\frac{L}{3} \end{aligned} \tag{9}$$

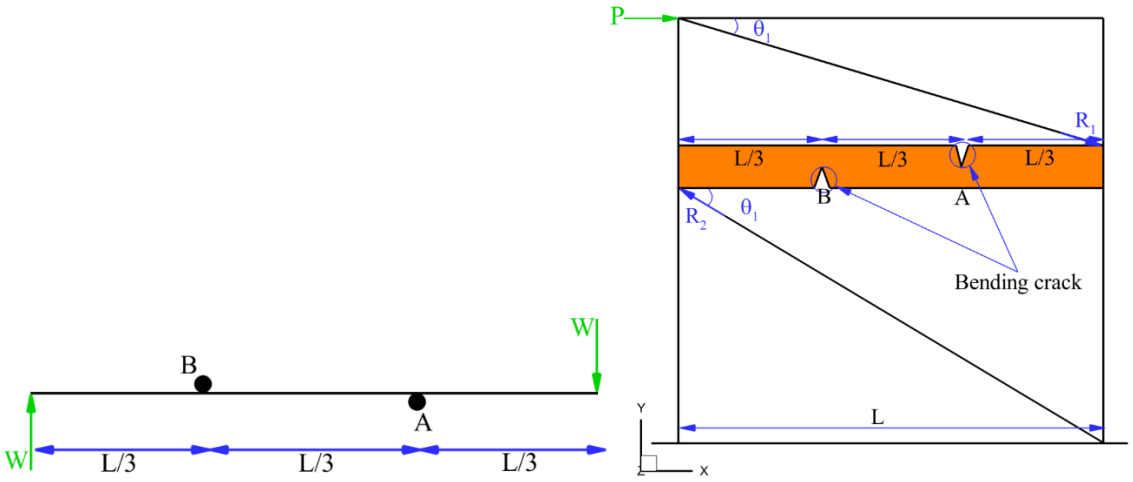


**Fig. 16.** a) Amount of load applied to the bond beam, b) Ideal mechanism for timber.

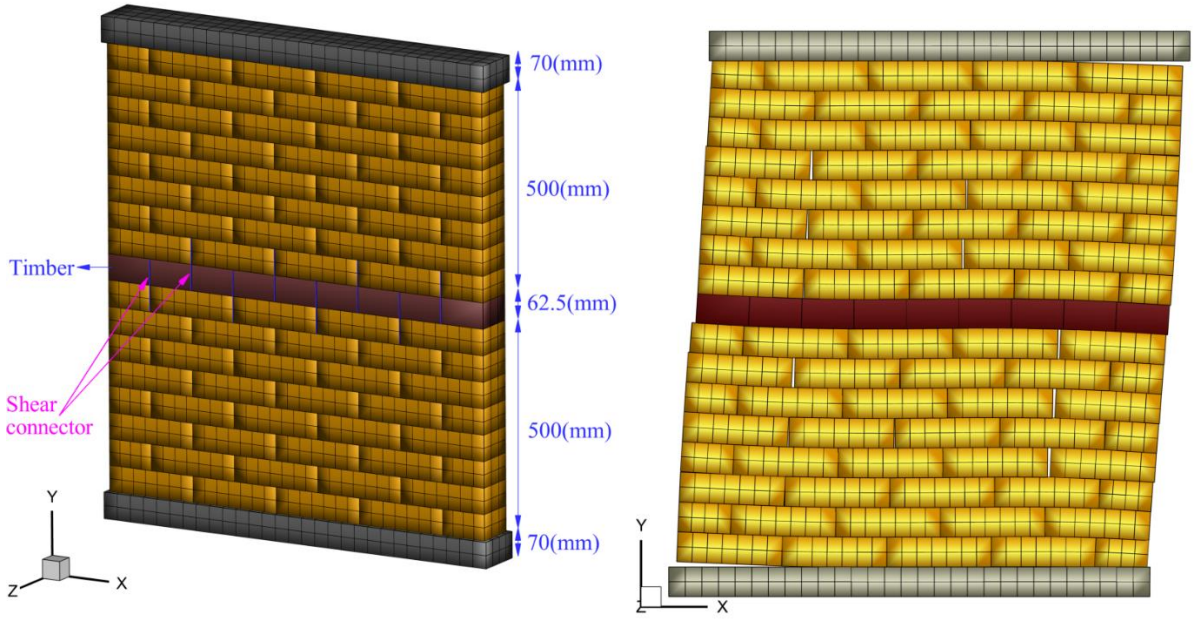


**Fig. 17.** a) A view of the numerical model and meshing procedure b) Deformation, cracking and sliding of wall in the last step of loading.

## 4.2. Vertical application of timber in the middle of the wall

In this part, the timber is placed vertically in the wall, so that its effect can be investigated. According to the structural wall reinforcement analysis in small displacements, vertical timber does not affect the wall behavior, and the wall behaves almost same as a non-reinforced wall.

As shown in Figure 19, the wall loses its strength at a load equivalent to 50KN (point A), and undergoes an unstable deformation. With an increase in wall displacement, the timber plays its role and withstands the lateral load same as a tensile member (point B). Therefore, given the type of cracking and load-displacement behavior of the reinforced wall, it is quite clear that vertical timber is not suitable for increasing the bear loading (the maximum initial load, point A, is approximately equal to the maximum load of the unreinforced wall).

However, this element takes effect after wall cracking and deformation, and prevents the roof from collapse and can withstand lateral force. This behavior is clearly shown in Figure 18. Accordingly, with the initial sliding of the wall, the stress on the timber increases, and the timber withstands the lateral force (R). Figure 18 shows a numerical model of the meshing, sliding and cracking patterns at the points A and B.

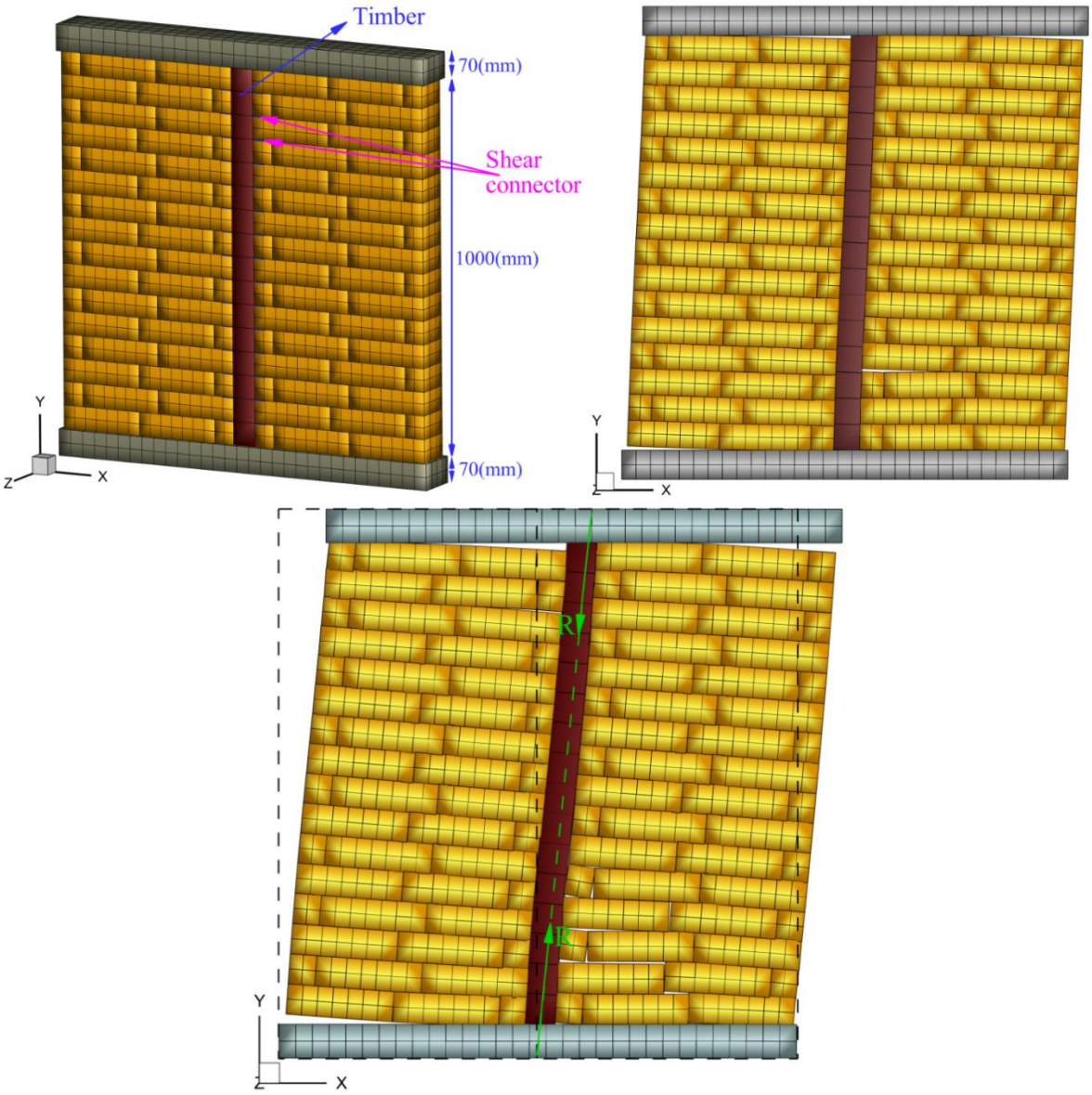


**Fig. 18.** A view of the numerical model and meshing procedure; b) Deformation of wall and its cracking and sliding at a) point A & b) Point B.

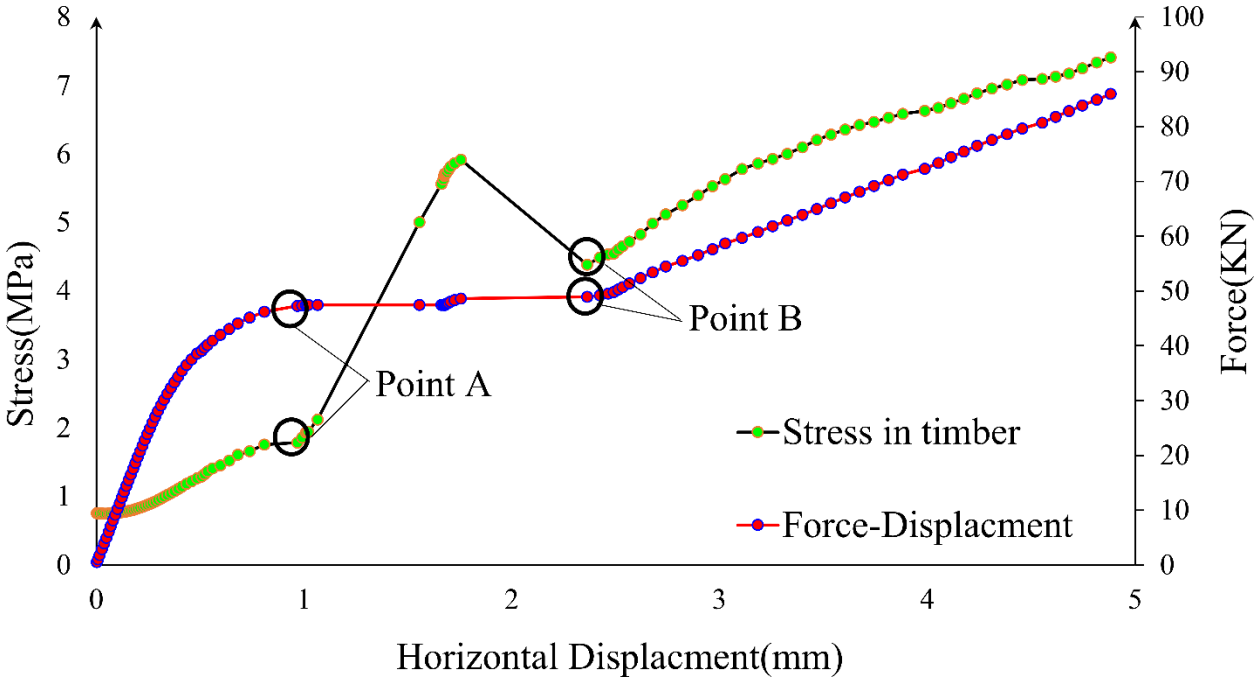


**Fig. 19.** Comparison of the stress applied to the vertical timber and amount of bearing force by the wall versus horizontal displacement.

## 4.3. Cross-shaped application of timber in the middle of the wall

In this part, by combining the two previous parts, the wall was reinforced with horizontal and vertical timber, and the connection of the two timbers to each other was modeled in a bending form.

The load-displacement diagram of this model (Figure 21) clearly indicates that the maximum load and wall ductility is considerably boosted.

The maximum wall load increases by 115KN at the point D. In addition, at the point D onwards, the vertical timber withstands the lateral force due to the considerable change in the wall, and prevents the collapse of the roof and he wall.

Due to the crosswise performance of the timber, the behavior of the wall will be almost the same as that of the infill.

It is clear from Figure 20 that the vertical timber withstands lateral force due to the loss in the wall lateral force and excessive deformation (point D), and the stress in this member increases.

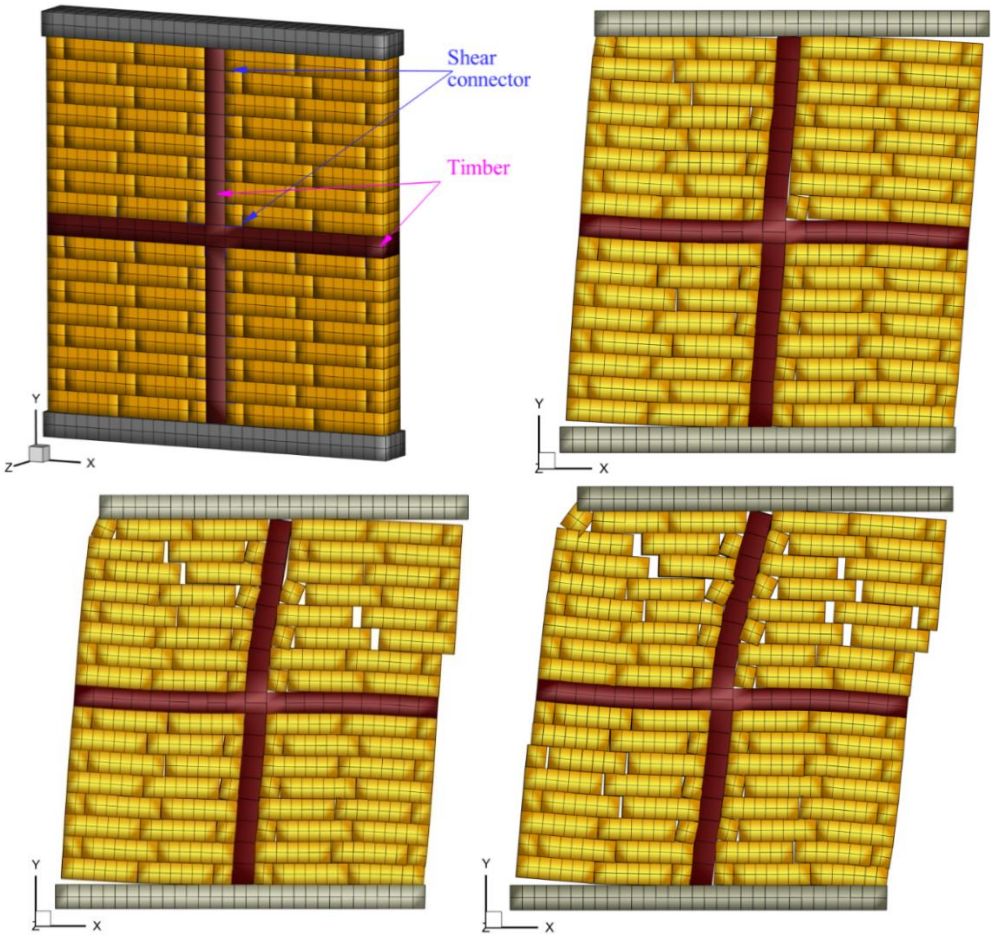


**Fig. 20.** A view of numerical model and meshing procedure b) Deformation, cracking and sliding of wall at points C, D, & E.

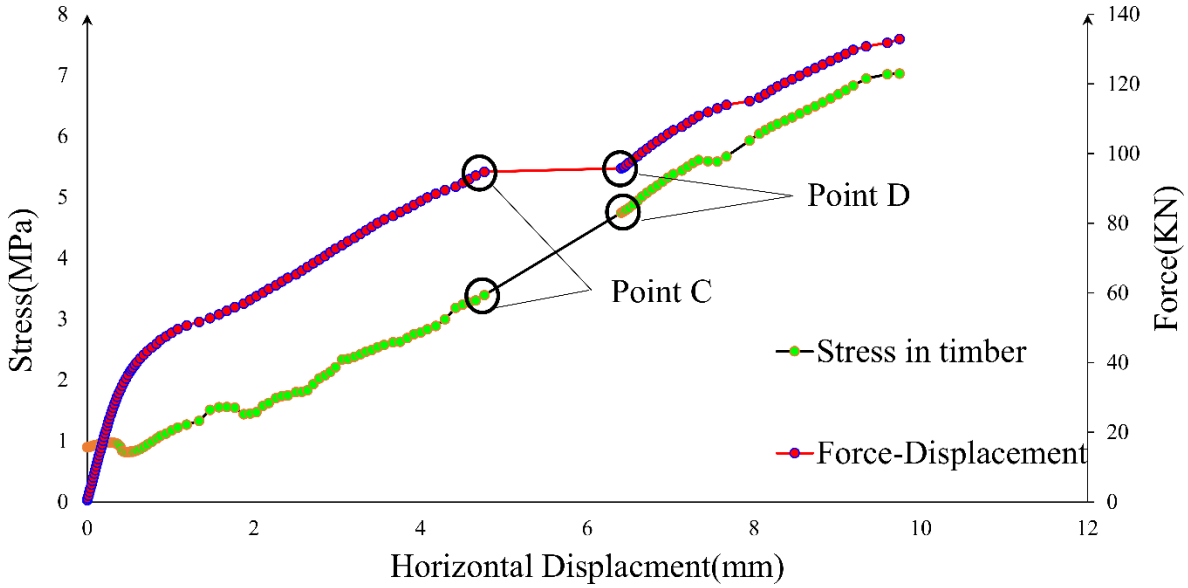


**Fig. 21.** Stress applied to timber and amount of force borne by the wall in comparison to horizontal displacement.

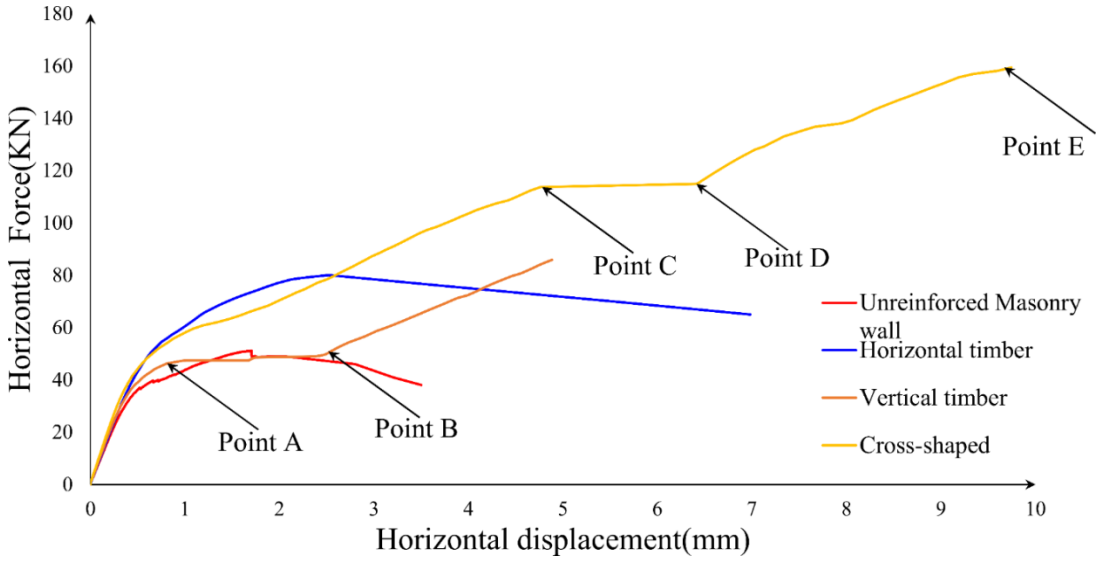


**Fig. 22.** Comparison of load-relocation diagram of reinforced walls vs. unreinforced walls.

Figure 22 compares the behavior of the reinforced and unreinforced walls.

## 5. Review ductility

Ductility is an important factor in evaluating the seismic behavior of a structure because it means the ability of the structure to withstand nonlinear deformation without losing much strength. Displacement ductility is attained by the ratio between ultimate displacement and yield displacement, and an equivalent bilinear diagram is required to calculate it. The equivalent bilinear diagram is a completely elastoplastic form of wall response.

### 5.1. Procedure to form an equivalent bilinear diagram

To obtain an equivalent bilinear diagram that represents the elastoplastic response of the wall, pushover curves relevant to each wall are specified. Pushover curves connect the maximum load points in a hysteresis diagram for each displacement.

Figure 22 presents the diagram of the unreinforced walls and the walls reinforced with timbers. It is stipulated that only positive displacements are shown in plotting the pushover curve and calculating the seismic performance parameters.

In FEMA 404 [29] as well as in Tomaz˘evic [30] some methodologies are proposed to determine bilinear diagrams. [30]considers the failure load to be 90% of the maximum load, and calculates the yield limit through the parity of the areas.

The mechanical quantity, which determines the load-bearing capacity and deformability of masonry walls, such as the ductility factor, $\mu_u$, should be determined experimentally by using testing procedures which are compatible with experiments on the basis of which equations for calculations are developed.

In order to make the calculations simple, the actual hysteretic behavior of a masonry wall, subjected to a combination of constant vertical load and a sequence of lateral load reversals is represented by an idealized bi- or trilinear resistance envelope. To idealize the experimental envelope, three limit states

in the observed behavior of the tested wall are first defined:

- Crack limit, determined by displacement $d_{cr}$and resistance $H_{cr}$at the formation of the first significant cracks in the wall, which change the slope of the envelope.
- Maximum resistance, determined by maximum resistance $H_{max}$, attained during test, and corresponding displacement $d_{Hmax}$,.
- Ultimate state, determined by maximum displacement attained during test $d_{max}$ and corresponding resistance $d_{Hmax}$.

Obviously, the initial slope of the idealized envelope is best defined with a secant stiffness at the formation of cracks, which is called effective stiffness of the wall $K_e$. It is calculated as the ratio between the resistance and displacement of the wall at crack limit: (Equation 10)

$$K_e = \frac{H_{cr}}{d_{cr}} \tag{10}$$

If the resistance envelope is idealised with a bilinear relationship, the ultimate resistance of the idealised envelope $H_u$ is evaluated by taking into account the equal energy dissipation capacity of an actual and idealised wall: the areas below the actual and idealised curves should be equal (Figure 23).

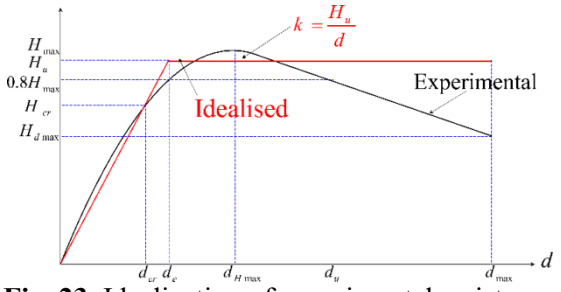


**Fig. 23.** Idealization of experimental resistance envelope with bilinear relationship.

When idealizing the experimental curve, and knowing the initial stiffness $K_e$, the ultimate resistance $H_u$ can be easily calculated from Equation 11:

$$H_u = K_e(d_{max} - \sqrt{d_{max}^2 - \frac{2A_{env}}{K_e}}) \tag{11}$$

where:

$A_{env}$= the area below the experimental resistance envelope. It should be emphasized, at this point, that ultimate resistance $H_u$ does not represent the design but the idealised maximum experimental value. An analysis of the results obtained from the testing of 60 walls indicates that, the average value ratio $H_u/H_{max}$ is 0.9. Consequently, in the case of bilinear idealization of resistance envelope, the calculated values of maximum resistance should be multiplied by 0.9: (equation 12)

$$H_u = 0 \cdot 9H_{max} \tag{12}$$

Arbitrarily, the ultimate idealised displacement $d_u$ is defined as the displacement value where the idealised line intersects the descending branch of the experimental one. Consequently, ultimate ductility factor (indicator) $\mu_u$ is defined as a ratio in equation 13:

$$\mu_u = \frac{d_u}{d_e} \tag{13}$$

and the displacement at the idealised elastic limit $d_e$ is evaluated from equation 14:

$$d_e = \frac{H_u}{K_e} \tag{14}$$

In seismic resistance verification, however, the value of ultimate ductility factor $\mu_u$ is limited to avoid excessive damage to structural walls.

Usually, allowable values for individual structural walls, which are taken into account in the calculations of the idealised

resistance envelopes of structural walls, are greater than the values of behavior factors recommended for each particular type of masonry construction. However, although experimental results might indicate that larger values could be acceptable, it is recommended that the values of ultimate ductility factor $\mu_u$ of individual walls are limited to:

- $\mu_u$ = 2.0-3.0 for the case of plain masonry walls.
- $\mu_u$ = 3.0-4.0 for the case of confined masonry walls.
- $\mu_u$ = 4.0-5.0 for the case of reinforced masonry walls.

Taking into account all the above, Table 6 presents the ductility values for the base unreinforced masonry walls and the walls reinforced by the timber.
If parameter A is the percentage increase in the ultimate strength of the reinforced walls relative to the unreinforced wall, and B is the percentage increase in the ductility of the reinforced walls relative to the unreinforced wall, the important function of the timber elements in increasing the ductility and ultimate strength of the improved walls can be clearly observed [31,32].

**Table 6.** Values of ductility and ultimate strength of walls.

| | μ | $f_u$ | A | B |
|---|---|---|---|---|
| UNREINFORCED WALL | 4.25 | 51 | | |
| VERTICAL WOOD | 5.22 | 85 | [(85-51)/51]×100=67 | [(5.22-4.25)/4.25]×100=22 |
| HORIZONTAL WOOD | 7.77 | 80 | [(80-51)/51]×100=56 | [(7.77-4.25)/4.25]×100=82 |
| CROSS SHAPED WOOD | 9.14 | 159 | [(159-51)/51]×100=211 | [(9.14-4.25)/4.25]×100=115 |

## 6. Conclusion

The present paper investigated experimental specimens of timber and its mechanical properties. Standard wood tests were used to determine mechanical properties. The modeling results of the timber specimens showed brittle behavior in tension and semi-ductile behavior in pressure.

After validating the numerical modeling of the timbers, masonry wall modelling methods were explicated, and out of macro and meso approaches, the meso approach was selected due to its higher accuracy. Then the masonry wall was retrofitted and strengthened by three different timber placement patterns.

The following results were obtained by examining the presented models:

1-Timber placement contributes to wall cracking variation and considerable improvement in ductility and shear capacity of wall.

2-Crosswise placement of the timber on the masonry wall exhibited the best seismic performance because it was accompanied by a 211% increase in ductility and 115% increase in ultimate strength, which such increase is very significant.

3- The results showed that masonry wall reinforcement technique using wooden elements is a valid traditional reinforcement method that has an acceptable ultimate

performance despite the low cost and lack of need to expertise or skills of workforce.

4- Note that the walls reinforced by this method are able to withstand more displacement due to their greater ductility than unreinforced walls.

## REFERENCES


[1] Tomasi, R. and Sartori, T. (2013). Mechanical behaviour of connections between wood framed shear walls and foundations under monotonic and cyclic load, Journal of Construction and Building Materials, 44: p. 682-690. DOI 10.1016/j.conbuildmat.2013.02.055.

[2] Seim, W., Hummel, J. and Vogt, T. (2014). Earthquake design of timber structures–Remarks on force-based design procedures for different wall systems. Journal of Engineering Structures, 76: p. 124-137. DOI 10.1016/j.engstruct.2014.06.037.

[3] Parisi, M.A. and Piazza, M. (2015). Seismic strengthening and seismic improvement of timber structures. Journal of Construction and Building Materials, 97: p. 55-66. DOI 10.1016/j.conbuildmat.2015.05.093.

[4] Steiger, R., et al., (2015). Strengthening of timber structures with glued-in rods. Journal of Construction and building materials, 97: p. 90-105. DOI 10.1016/j.conbuildmat.2015.03.097.

[5] Anil, Ö., et al., (2016). Hysteretic behavior of timber framed shear wall with openings. Journal of Construction and Building Materials, 116: p. 203-215. DOI 10.1016/j.conbuildmat.2016.04.068.

[6] Bedon, C., Rinaldin, G. and Fragiacomo, M. (2015). Non-linear modelling of the in-plane seismic behaviour of timber Blockhaus log-walls. Journal of Engineering Structures, 91: p. 112-124. DOI 10.1016/j.engstruct.2015.03.002.

[7] Guíñez, F., Santa María, H. and Almazán, J.L. (2019). Monotonic and cyclic behaviour of wood frame shear walls for mid-height timber buildings. Journal of Engineering Structures, 189: p. 100-110. DOI 10.1016/j.engstruct.2019.03.043.

[8] Ceroni, F. and Di Ludovico, M. (2020). Traditional and innovative systems for injected anchors in masonry elements: Experimental behavior and theoretical formulations. Journal of Construction and Building Materials, 254: p. 119178. DOI 10.1016/j.conbuildmat.2020.119178.

[9] Estrella, X., et al., (2020). Efficient nonlinear modeling of strong wood frame shear walls for mid-rise buildings. Journal of Engineering Structures, 215: p. 110670. DOI 10.1016/j.engstruct.2020.110670.

[10] Carrero, T., et al., (2020). Static and dynamic performance of direct hybrid connections of cross-laminated timber with steel, concrete and laminated strand lumber composites. Latin American Journal of Solids and Structures, 17(4). DOI 10.1590/1679-78256106 .

[11] Marzaleh, A.S., et al., (2018). OSB sheathed light-frame timber shear walls with strong anchorage subjected to vertical load, bending moment, and monotonic lateral load. Journal of Engineering Structures, 173: p. 787-799. DOI 10.1016/j.engstruct.2018.05.044.

[12] Jayamon, J.R., Line, P. and Charney, F.A. (2018). State-of-the-art review on damping in wood-frame shear wall structures. American Society of Civil Engineers. DOI 10.1061/(ASCE)ST.1943541X.0002212.

[13] Casagrande, D., et al., (2020). A methodology to determine the seismic low-cycle fatigue strength of timber connections. Journal of Construction and Building Materials, 231: p. 117026. DOI 10.1016/j.conbuildmat.2019.117026.

[14] Standard, A., D143. (2014). Standard Test Methods for Small Clear Specimens of Timber. West Conshohocken, PA: ASTM International. DOI 10.1520/D0143-14.

[15] Green, D.W., Winandy, J.E. and Kretschmann, D.E. (1999). Mechanical properties of wood. Wood handbook:

wood as an engineering material. Madison, WI: USDA Forest Service, Forest Products Laboratory, General technical report FPL; GTR-113: Pages 4.1-4.45.

[16] Hong, J.-P., (2007). Three-dimensional nonlinear finite element model for single and multiple dowel-type wood connections. University of British Columbia. DOI 10.14288/1.0066597.

[17] Kouris, L.A.S. and Kappos, A.J.,(2012). Detailed and simplified non-linear models for timber-framed masonry structures. Journal of Cultural Heritage, 13(1), p.47-58. DOI 10.1016/j.culher.2011.05.009.

[18] Vermeltfoort, A.T., T. Raijmakers, and Janssen, H. (1993). Shear tests on masonry walls.

[19] Akhaveissy, A., (2013). Limit state strength of unreinforced masonry structures. Journal of Earthquake spectra, 29(1): p. 1-31. DOI 10.1193/1.4000097.

[20] Petracca, M., et al., (2017). Micro-scale continuous and discrete numerical models for nonlinear analysis of masonry shear walls. Journal of Construction and Building Materials, 149: p. 296-314. DOI 10.1016/j.conbuildmat.2017.05.130.

[21] Menetrey, P., (1994). Numerical analysis of punching failure in reinforced concrete structures. EPFL. DOI 10.5075/epfl-thesis-1279.

[22] Menétrey, P., (2002). Synthesis of punching failure in reinforced concrete. Cement and Concrete Composites, 24(6): p. 497-507. DOI 10.1016/S0958-9465(01)00066-X.

[23] Alfano, G. and Crisfield, M.A. (2001). Finite element interface models for the delamination analysis of laminated composites: mechanical and computational issues. International journal for numerical methods in engineering, 50(7): p. 1701-1736. DOI 10.1002/nme.93.

[24] Park, K. and Paulino, G.H. (2011). Cohesive zone models: a critical review of traction-separation relationships across fracture surfaces. Journal of Applied Mechanics Reviews, 64(6). DOI 10.1115/1.4023110.

[25] Nguyen, V.P., et al., (2017). Modelling hydraulic fractures in porous media using flow cohesive interface elements. Journal of Engineering Geology, 225: p. 68-82. DOI 10.1016/j.enggeo.2017.04.010.

[26] Feng, D.-C. and Wu, J.-Y. (2018). Phase-field regularized cohesive zone model (CZM) and size effect of concrete. Journal of Engineering Fracture Mechanics, 197: p. 66-79. DOI 10.1016/j.engfracmech.2018.04.038.

[27] Yang, Z.-J., Li, B.-B. and Wu, J.-Y. (2019). X-ray computed tomography images based phase-field modeling of mesoscopic failure in concrete. Journal of Engineering Fracture Mechanics, 208: p. 151-170. DOI 10.1016/j.engfracmech.2019.01.005.

[28] Roland, J.P.A.K.B. and Wenk, B.T. (2020). Characterization of mortar–timber and timber–timber cyclic friction in timber floor connections of masonry buildings. Materials and Structures, 53: p. 51. DOI 10.5281/zenodo.3348328.

[29] FEMA, A., *440*, (2005). Improvement of nonlinear static seismic analysis procedures. FEMA-440, Redwood City, **7**(9): p. 11.

[30] Tomaževič, M., Earthquake-resistant design of masonry buildings. 1999: World Scientific. DOI 10.1142/p055.

[31] Mohammadi Nikou, M., Akhaveissy, A., (2018). Evaluation of the seismic performance of masonry walls reinforced with wooden elements. Journal of Structural and Construction Engineering, 5(2),p. 113-133. DOI 10.22065/jsce.2017.86039.1175

[32] Mohamadi Nikou, M., Ahakhaveissy, A., (2019). The role of wooden elements for improving seismic performance and cracking paterns of masonry walls. Sharif Journal of Civil Engineering, 35.2(2.2),p. 143-152. DOI 10.24200/j30.2018.1845.1981.